

# Matched Filtering-Based Channel Estimation for AFDM Systems in Doubly Selective Channels

Xiangjun Li, Zilong Liu, Zhengchun Zhou, and Pingzhi Fan

**Abstract**—Affine frequency division multiplexing (AFDM) has recently emerged as an excellent backward-compatible 6G waveform. In this paper, an enhanced AFDM is proposed whereby the delay-Doppler (DD) coupling phase is considered. Specifically, we study matched filtering (MF) assisted channel estimation (CE) for AFDM systems in complex doubly selective channels. By deriving the complete input-output relationship, the inter-chirp-carrier interference, signal-to-interference-plus-noise ratio (SINR), and the effective SINR loss of AFDM, are investigated in discrete affine Fourier transform (DAFT) domain. Further, we look into the path ambiguity problem and show that it may lead to severe performance deterioration in fractional-delay fractional-Doppler channels. To address such a problem, we introduce an MF assisted CE scheme building upon a novel pilot arrangement across two consecutive AFDM transmissions. This allows us to sequentially estimate the parameters of each path by exploiting the separability and approximate orthogonality of different paths in the DAFT domain, thus leading to significantly reduced complexity. Furthermore, based on generalized Fibonacci search (GFS), an MF-GFS scheme is proposed to avoid significantly redundant computation, which can be extended to typical wide-band systems. Extensive simulation results indicate that the proposed schemes offer superior advantages in terms of their improved communication performance and lower complexity.

**Index Terms**—Affine frequency division multiplexing (AFDM), channel estimation, doubly selective channels, matched filtering.

## I. INTRODUCTION

THE sixth generation (6G) communication systems are deemed to support ultra-reliable, low-latency, and high-rate communications in highly dynamic scenarios, such as vehicle-to-everything (V2X) systems, unmanned aerial vehicles, high-speed trains, and low-earth-orbit (LEO) satellites. Traditional orthogonal frequency-division multiplexing (OFDM) may be infeasible due to significant inter-carrier interference caused by high mobility [1]–[3].

Several waveforms that can adapt to high-mobility scenarios have been studied. Among many others, a representative waveform is orthogonal time-frequency space (OTFS) whose information symbols are transmitted in the delay-Doppler (DD) domain through two-dimensional (2D) orthogonal basis functions [4]–[7]. Since each information symbol in the DD domain spans the entire time-frequency grid, OTFS is able to achieve a significant improvement in error rate performance compared to OFDM [6]–[13]. However, OTFS requires radical

change for the transceiver design and hence may not permit a seamless integration of the legacy OFDM based wireless systems.

Recently, affine frequency division multiplexing (AFDM) has emerged as an excellent backward-compatible 6G waveform for efficient and reliable high-mobility communications [13]–[15]. With minimum modification of OFDM, AFDM modulates the data symbols using multiple orthogonal chirp-carriers. The modulation is carried out through discrete affine Fourier transform (DAFT), enabling efficient mapping between the DAFT domain and the time domain. By appropriately tuning the chirp rate according to the Doppler profile of the channel, AFDM enables proper spreading in the time-frequency domain, thus allowing it to achieve the full diversity over the doubly selective channels. Besides, the sparsity and compactness of the channel in the DAFT domain can be exploited for reducing the pilot overhead. Special cases of AFDM include DAFT-OFDM [16] and orthogonal chirp division multiplexing (OCDM) [17], yet they may not be able to achieve the full diversity [15].

A plethora of recent works have further explored AFDM. Inspired by the index modulation (IM) for OFDM [18], IM-AFDM systems were studied in [19]–[22] for improving the spectrum efficiency. The integration of generalized spatial modulation (GSM) and AFDM, called GSM-AFDM, was studied in [23] to design low-power and high-performance multiple-input and multiple-output (MIMO) systems. For 6G integrated sensing and communications (ISAC), several studies demonstrated the advantages of AFDM empowered ISAC [24]–[26] systems. To support massive machine-type high-mobility communications, AFDM was also exploited as the building waveform for sparse code multiple access (SCMA) systems in [27].

Most existing works assume that the receiver has perfect channel information to achieve excellent transmission performance. In practice, however, channel estimation (CE) is generally required for coherent receiving systems. Similar to the traditional CE scheme in OTFS [9], the least square (LS) estimator was investigated in [28] along with a reasonable threshold to estimate the path parameters. By exploiting the sparsity of the channel, the authors in [29]–[31] modeled CE as a sparse signal recovery problem and estimated the channel using the compressed sensing (CS) algorithm.

The aforementioned schemes mostly assume that the normalized delay and Doppler values of the paths are integers. Nevertheless, the real-life channel response of each path typically does not align with the grid point in the DAFT domain. That is, the normalized delay and Doppler values

Xiangjun Li, Zhengchun Zhou and Pingzhi Fan are with the School of Info Sci & Tech, Southwest Jiaotong University, Chengdu, China. Zilong Liu is with the School of Computer Science and Electronics Engineering, University of Essex, U. K. Corresponding author: Zhengchun Zhou. Emails: lxj@my.swjtu.edu.cn; zilong.liu@essex.ac.uk; zzc@swjtu.edu.cn; pzf-fan@swjtu.edu.cn.

may have fractional components, potentially resulting in loss of channel sparsity, as well as degradation of CE performance in the DAFT domain. To address this issue, a CE scheme for MIMO-AFDM based on the diagonal reconstruction of the subchannel matrix was proposed in [32]. Their scheme directly estimates the effective channel matrix instead of the specific channel parameters. An approximate maximum likelihood CE scheme for AFDM was proposed in [15] by assuming that the delay of each propagation path is different and the number of paths is known *a priori*. In addition, the joint estimation of all paths in [15] results in a high computational complexity.

Against the above background, this work investigates matched filtering (MF) assisted CE schemes in doubly selective channels for AFDM systems. We differentiate integer-delay-fractional-Doppler (IDFD) and fractional-delay-fractional-Doppler (FDFD) channels and develop advanced MF-CE schemes through the co-design of transmit pilot signals and receiver signal processing. The main contributions are summarized as follows:

- Firstly, we adopt the input-output (I/O) relationship in the time domain, in alignment with that employed in existing OTFS-related research. We derive the corresponding I/O relationship in the DAFT domain and then present a comprehensive analysis on the inter-chirp-carrier-interference (ICCI), signal-to-interference-plus-noise ratio (SINR) and effective SINR loss.
- Secondly, we present the first analysis of the path ambiguity problem<sup>1</sup> in FDFD channels, where the inability to accurately estimate the delay and Doppler values of a path leads to significant degradation in CE performance. Motivated by this, a new pilot pattern and an MF scheme are proposed. The key idea is to use the different equivalent shifts of a path in the two AFDM symbols with different chirp rates to uniquely determine the delay and Doppler values<sup>2</sup>. In addition, by leveraging the separability and orthogonality of different paths, our proposed MF scheme is able to eliminate the matrix inversion operation, decouple joint estimation, and narrow the search range, thus leading to significantly reduced CE complexity.
- Thirdly, based on the generalized Fibonacci search (GFS) algorithm [35]–[37], we propose an MF-GFS CE scheme for FDFD channels. It is found that our proposed scheme can reduce the amount of search when estimating fractional parameters, yielding a significant reduction of redundant computations whilst outperforming the proposed MF scheme.
- Finally, we extend the proposed MF CE to the IDFD channels in typical wide-band systems (i.e., millimeter-wave communication systems) whereby the bandwidth is sufficiently large to approximate the normalized delay shifts to be integers. Given that the objective function for estimating fractional Doppler can also be demonstrated to

be unimodal, an MF-GFS scheme is proposed for IDFD channels. Simulation results indicate that the proposed schemes offer advantages in both computational complexity and performance.

The rest of this paper is organized as follows. Section II reviews the basic concepts of AFDM. Section III analyzes the I/O relationship, ICCI, SINR, and effective SINR loss of the AFDM system. Section IV introduces the MF CE scheme and MF-GFS CE scheme. Section V gives the simulation results. Finally, Section VI concludes this paper.

## II. SYSTEM MODELS

### A. AFDM modulation

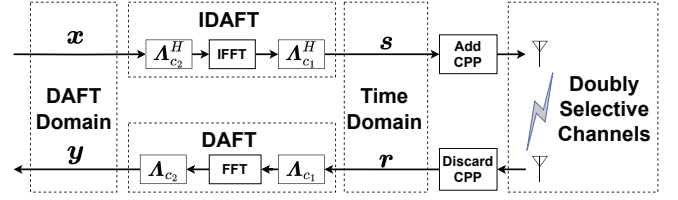


Fig. 1: AFDM system block diagram.

Assume that the number of chirp subcarriers is  $N$ , the subcarrier spacing is  $\Delta f$  (Hz), the bandwidth is  $B = N\Delta f$ , and the duration of an AFDM symbol is  $T$ . The DAFT domain axis is sampled at multiple times of  $\Delta f$  to obtain a discrete grid, i.e.,  $\Xi = \{n\Delta f, n = 0, \dots, N-1\}$ . In this paper, the AFDM system is illustrated in Fig. 1. For the transmitter (TX) side, consider a set of  $N$  information symbols  $\{x(n), n = 0, \dots, N-1\}$  from a modulation alphabet  $\mathbb{A}$  of size  $M_{\text{mod}}$  (e.g. QAM symbols), which are arranged on the DAFT domain grid  $\Xi$ . The AFDM modulator first employs inverse DAFT (IDAFT) to map  $x(n)$  to  $s(\bar{n})$ , as shown below:

$$s(\bar{n}) = \sum_{n=0}^{N-1} x(n) F_{c_1, c_2}(\bar{n}, n), \quad (1)$$

where  $F_{c_1, c_2}(\bar{n}, n) = \frac{1}{\sqrt{N}} e^{j2\pi(c_1 \bar{n}^2 + c_2 n^2 + \frac{\bar{n}n}{N})}$ ,  $\bar{n} \in \{0, \dots, N-1\}$  is the time index,  $n \in \{0, \dots, N-1\}$  is the chirp subcarrier index in the DAFT domain,  $c_1$  and  $c_2$  are DAFT parameters. Note that AFDM achieves full diversity in doubly selective channels if  $c_1$  satisfies [15]

$$c_1 = \frac{2(k_{\max} + \xi) + 1}{2N}, \quad (2)$$

where integer  $\xi$  satisfies  $0 < \xi \leq N$ . (1) can be rewritten as

$$\mathbf{s} = \mathbf{A}^H \mathbf{x}, \quad (3)$$

where  $\mathbf{x} = [x(0), \dots, x(N-1)]^T \in \mathbb{C}^{N \times 1}$ ,  $\mathbf{s} = [s(0), \dots, s(N-1)]^T \in \mathbb{C}^{N \times 1}$ ,  $\mathbf{A} = \Lambda_{c_2} \mathbf{F} \Lambda_{c_1}$  is the normalized DAFT matrix,  $\mathbf{F}$  is the normalized DFT matrix,  $\Lambda_c = \text{diag}(e^{-j2\pi cn^2}, n = 0, 1, \dots, N-1)$ ,  $(\cdot)^T$  is the transpose operation,  $(\cdot)^H$  is the conjugate transpose operation,  $\text{diag}(\cdot)$  is to convert a vector into a diagonal matrix or extract the diagonal elements of a matrix. Before transmission, a chirp-periodic prefix (CPP) [15] of length  $L_{\text{CPP}}$  is also employed.

<sup>1</sup>As we will show later, (37) becomes invalid for FDFD channels, thus resulting in path ambiguity.

<sup>2</sup>Specifically, the same path exhibits different equivalent shifts in two AFDM symbols with different chirp rates. The path ambiguity problem can be resolved by estimating the two equivalent shifts with additional pilot overhead.

### B. Doubly Selective Channels

Considering the sparsity of the channel, the channel response  $h(\tau, \nu)$  can be expressed as

$$h(\tau, \nu) = \sum_{i=1}^P h_i \delta(\nu - \nu_i) \delta(\tau - \tau_i), \quad (4)$$

where  $h_i, \tau_i \in [0, \tau_{\max}]$  and  $\nu_i \in [-\nu_{\max}, \nu_{\max}]$  are the channel gain, delay and Doppler parameters of the  $i$ -th path, respectively,  $\delta(\cdot)$  is the Dirac delta function,  $P$  is the number of paths.  $\nu_{\max}$  and  $\tau_{\max}$  are the maximum Doppler and delay, respectively. The normalized delay  $l_{\tau_i}$  and Doppler  $k_{\nu_i}$  satisfy

$$\tau_i = \frac{l_{\tau_i}}{N\Delta f}, \quad \nu_i = k_{\nu_i} \Delta f, \quad (5)$$

where  $k_{\nu_i} = \bar{k}_{\nu_i} + \kappa_{\nu_i} \in [-k_{\max}, k_{\max}]$ ,  $l_{\tau_i} = \bar{l}_{\tau_i} + \iota_{\tau_i} \in [0, l_{\max}]$ ,  $\bar{k}_{\nu_i}$  and  $\bar{l}_{\tau_i}$  are both integer parts,  $\kappa_{\nu_i} \in [-0.5, 0.5]$  and  $\iota_{\tau_i} \in [-0.5, 0.5]$  are both fractional parts,  $k_{\max} = \lceil \frac{N\nu_{\max}}{B} \rceil$ ,  $l_{\max} = \lceil \tau_{\max} B \rceil$ , the ceiling function  $\lceil \cdot \rceil$  returns the smallest integer greater than the input value. Due to the finite  $B$  and  $T$ , there is generally fractional delay and Doppler.  $\nu_{\max}$  and  $\tau_{\max}$  can usually be considered known a priori [10]. However, the number of scatterers in the environment is usually unpredictable, resulting in the uncertainty of  $P$ .

After digital-to-analog conversion, the transmitted signal is represented by  $s(t)$ . In [15], the received signal  $r(t)$  is

$$r(t) = \iint h(\tau, \nu) s(t - \tau) e^{j2\pi\nu t} d\tau d\nu + \tilde{w}(t), \quad (6)$$

However, to be consistent with existing OTFS-related research,  $r(t)$  in this paper is given by [4]

$$r(t) = \iint h(\tau, \nu) s(t - \tau) e^{j2\pi\nu(t-\tau)} d\tau d\nu + \tilde{w}(t), \quad (7)$$

where  $\tilde{w}(t)$  is the additive white Gaussian noise. The two interpretations of the channel impulse response differ by a term  $e^{-j2\pi\nu\tau}$ . As long as the notation is consistent, equivalent results can be obtained by using either definition.

Substitute (4) into (7), and consider  $r(t)$  which is sampled at multiples of  $T_s = \frac{1}{N\Delta f} = \frac{T}{N}$ . After discarding CPP, the vector  $\mathbf{r} = [r(0), \dots, r(N-1)]^T \in \mathbb{C}^{N \times 1}$  is

$$r(\bar{n}) = \sum_{i=1}^P h_i s(\bar{n} - l_{\tau_i}) e^{\frac{j2\pi k_{\nu_i}}{N} (\bar{n} - l_{\tau_i})} + \tilde{w}(\bar{n}). \quad (8)$$

where the noise  $\tilde{w}(\bar{n})$  follows  $\mathcal{CN}(\tilde{w}(\bar{n}) | 0, \lambda^{-1})$ ,  $\lambda$  is the noise accuracy. (8) can be expressed in matrix form as

$$\mathbf{r} = \mathbf{H}_T \mathbf{s} + \tilde{\mathbf{w}}, \quad (9)$$

where  $\mathbf{H}_T = \sum_{i=1}^P h_i \mathbf{\Gamma}_{\text{CPP}_i} \mathbf{\Pi}^{l_{\tau_i}} \mathbf{\Delta}^{k_{\nu_i}} \in \mathbb{C}^{N \times N}$  is the channel matrix in the time domain,  $\mathbf{\Delta} = \text{diag}(z^0, z^1, \dots, z^{N-1}) \in \mathbb{C}^{N \times N}$ ,  $z = e^{j\frac{2\pi}{N}}$ ,  $\mathbf{\Pi} \in \mathbb{C}^{N \times N}$  is the forward cyclic-shift matrix,  $\mathbf{\Gamma}_{\text{CPP}_i} \in \mathbb{C}^{N \times N}$  is used to model CPP [15]. The delay and Doppler values are modeled by  $\mathbf{\Pi}$  and  $\mathbf{\Delta}$ , respectively.

### C. AFDM Demodulation

At the receiver side, the sample  $r(n)$  is processed by DAFT to obtain  $y(m)$  in the DAFT domain, i.e.,

$$y(m) = \sum_{\bar{n}=0}^{N-1} r(\bar{n}) F_{c_1, c_2}^*(\bar{n}, m) + w(m), \quad (10)$$

where  $(\cdot)^*$  is the conjugate operation. The distribution of the noise  $w(m)$  remains invariant. (10) can be rewritten as

$$\mathbf{y} = \mathbf{A} \mathbf{r} = \mathbf{H}_{\text{eff}} \mathbf{x} + \mathbf{w}, \quad (11)$$

where  $\mathbf{y} = [y(0), \dots, y(N-1)]^T \in \mathbb{C}^{N \times 1}$ ,  $\mathbf{H}_{\text{eff}} = \sum_{i=1}^P h_i \mathbf{A} \mathbf{\Gamma}_{\text{CPP}_i} \mathbf{\Pi}^{l_{\tau_i}} \mathbf{\Delta}^{k_{\nu_i}} \mathbf{A}^H \in \mathbb{C}^{N \times N}$  is the effective channel matrix in the DAFT domain.

## III. ANALYSIS OF I/O, ICCI AND SINR LOSS

### A. I/O Relation of AFDM

**Theorem 1.** The  $y(m)$  can be expressed as

$$y(m) = \sum_{n=0}^{N-1} x(n) h_w(m, n) + w(n), \quad (12)$$

$$h_w(m, n) = \sum_{i=1}^P h_i \mathcal{G}(m, n, k_{\nu_i}, l_{\tau_i}), \quad (13)$$

$$\mathcal{G}(m, n, k_{\nu_i}, l_{\tau_i}) = \alpha(m, n, k_{\nu_i}, l_{\tau_i}) \mathcal{F}(m, n, k_{\nu_i}, l_{\tau_i}), \quad (14)$$

$$\alpha(m, n, k_{\nu_i}, l_{\tau_i}) = e^{\frac{-j2\pi}{N} (-Nc_1 l_{\tau_i}^2 + (n + k_{\nu_i}) l_{\tau_i} + Nc_2 (m^2 - n^2))}, \quad (15)$$

and  $\mathcal{F}(m, n, k_{\nu_i}, l_{\tau_i})$  is given by (64).

*Proof:* The proof is given in Appendix A. ■

Rewriting (12) into another matrix form, we have

$$\mathbf{y} = \sum_{i=1}^P h_i \mathbf{H}_i \mathbf{x} + \mathbf{w}, \quad (16)$$

where  $\mathbf{H}_i = \mathbf{A} \mathbf{\Gamma}_{\text{CPP}_i} \mathbf{\Pi}^{l_{\tau_i}} \mathbf{\Delta}^{k_{\nu_i}} \mathbf{A}^H$ .

### B. ICCI Analysis

1) *Integer Delay-Doppler (IDD) Channels:* In this case,  $l_{\tau_i} = \bar{l}_{\tau_i}$ ,  $k_{\nu_i} = \bar{k}_{\nu_i}$ . Then the I/O relation in (12) will be simplified to

$$y(m) = \sum_{i=1}^P h_i \alpha(m, n, k_{\nu_i}, l_{\tau_i}) x(n) + w(n), \quad (17)$$

where  $n = [m + 2Nc_1 l_{\tau_i} - k_{\nu_i}]_N$ ,  $[\cdot]_N$  is the mod- $N$  operation. For the  $i$ -th path, since only the transmitted signal  $x([m + 2Nc_1 l_{\tau_i} - k_{\nu_i}]_N)$  constitutes  $y(m)$ , there is no ICCI for the IDD channels.

2) *IDFD Channels:* In this case,  $l_{\tau_i} = \bar{l}_{\tau_i}$ ,  $k_{\nu_i} = \bar{k}_{\nu_i} + \kappa_{\nu_i}$ . Due to the existence of fractional Doppler  $\kappa_{\nu_i}$ ,  $\mathcal{F}(m, n, k_{\nu_i}, l_{\tau_i})$  will not be zero for a given  $m$  and any  $n$ . Some works have shown that  $|\mathcal{F}(m, n, k_{\nu_i}, l_{\tau_i})|$  has a peak at  $n = [m + 2Nc_1 l_{\tau_i} - \bar{k}_{\nu_i}]_N$  and decreases significantly as  $n$  moves away from  $[m + 2Nc_1 l_{\tau_i} - \bar{k}_{\nu_i}]_N$ . Therefore, we only need to consider the  $2\xi + 1$  principal values of  $\mathcal{F}(m, n, k_{\nu_i}, l_{\tau_i})$  around the peak of

$[m + 2Nc_1l_{\tau_i} - \bar{k}_{\nu_i}]_N$ , i.e.,  $[m + 2Nc_1l_{\tau_i} - \bar{k}_{\nu_i} - \xi]_N \leq n \leq [m + 2Nc_1l_{\tau_i} - \bar{k}_{\nu_i} + \xi]_N$ . Based on this good approximation, we can re-express  $y(m)$  in (12) as

$$\begin{aligned} y(m) &\approx \sum_{i=1}^P \sum_{n=[m+2Nc_1l_{\tau_i}-\bar{k}_{\nu_i}-\xi]_N}^{[m+2Nc_1l_{\tau_i}-\bar{k}_{\nu_i}+\xi]_N} x(n)h_i\mathcal{G}(m,n,k_{\nu_i},l_{\tau_i}) \\ &\approx \sum_{i=1}^P \sum_{q=-\xi}^{\xi} x(n_q)h_i\alpha(m,n_q,k_{\nu_i},l_{\tau_i}) \\ &\quad \times \frac{e^{-j2\pi(q-\kappa_{\nu_i})} - 1}{Ne^{-j\frac{2\pi}{N}(q-\kappa_{\nu_i})} - N}, \end{aligned} \quad (18)$$

where  $n_q = [m - q + 2Nc_1l_{\tau_i} - \bar{k}_{\nu_i}]_N$ .

3) *FDFD Channels*: In this case,  $l_{\tau_i} = \bar{l}_{\tau_i} + \iota_{\tau_i}$ ,  $k_{\nu_i} = \bar{k}_{\nu_i} + \kappa_{\nu_i}$ . We rewrite  $\mathcal{F}(m,n,k_{\nu_i},l_{\tau_i})$  as follows

$$\begin{aligned} \mathcal{F}(m,n,k_{\nu_i},l_{\tau_i}) &= \frac{1}{N} \frac{e^{-j2\pi(m-n+2Nc_1(\bar{l}_{\tau_i}+\iota_{\tau_i})-\bar{k}_{\nu_i}-\kappa_{\nu_i})} - 1}{e^{-j\frac{2\pi}{N}(m-n+2Nc_1(\bar{l}_{\tau_i}+\iota_{\tau_i})-\bar{k}_{\nu_i}-\kappa_{\nu_i})} - 1} \\ &= \frac{1}{N} \frac{e^{-j2\pi(m-n-\chi_i)} - 1}{e^{-j\frac{2\pi}{N}(m-n-\chi_i)} - 1} \\ &= \mathcal{J}(m,n,\chi_i), \end{aligned} \quad (19)$$

where  $\Upsilon_i = \lfloor \chi_i \rfloor$  and  $\gamma_i = \chi_i - \Upsilon_i \in [-0.5, 0.5]$  are the integer and fractional parts of equivalent shift  $\chi_i$ , respectively,  $\chi_i = -2Nc_1l_{\tau_i} + k_{\nu_i}$ ,  $\lfloor \cdot \rfloor$  is the round operation. Due to the existence of fractional part  $\gamma$ , we also consider the principal values of  $\mathcal{J}(m,n,\chi_i)$  within the range of  $[m - \Upsilon_i - \xi]_N \leq n \leq [m - \Upsilon_i + \xi]_N$ . Therefore,  $y(m)$  can be approximated as

$$\begin{aligned} y(m) &\approx \sum_{i=1}^P \sum_{q=-\xi}^{\xi} x(n_q)h_i\alpha(m,n_q,k_{\nu_i},l_{\tau_i}) \\ &\quad \frac{e^{-j2\pi(q-\gamma_i)} - 1}{Ne^{-j\frac{2\pi}{N}(q-\gamma_i)} - N} + w(m), \end{aligned} \quad (20)$$

where  $n_q = [m - q - \Upsilon_i]_N$ . From (18) and (20), it is evident that  $y(m)$  is approximately a linear combination of  $P(2\xi + 1)$  transmitted signals. For the  $2\xi + 1$  transmitted signals in the  $i$ -th path, only  $x(n_{q|q=0})$  is the main source of  $y(m)$ , and the other  $2\xi$  signals can be regarded as interference. This interference is caused by the chirp-subcarriers near the  $n_{q|q=0}$ -th chirp-subcarrier, so it is called ICCI.

### C. SINR

For the receiver, linear minimum mean square error (LMMSE) equalization is used for  $\mathbf{y}$  to mitigate the effects of noise and interference, i.e.,  $\hat{\mathbf{x}} = \mathbf{W}\mathbf{y}$ , where  $\hat{\mathbf{x}}$  is the estimate of  $\mathbf{x}$ ,  $\mathbf{W} = (\mathbf{H}_{\text{eff}}^H \mathbf{H}_{\text{eff}} + \sigma^2 \mathbf{I}_N)^{-1} \mathbf{H}_{\text{eff}}^H$ . The signal of the  $n$ -th chirp-subcarrier is

$$\hat{x}(n) = \{\mathbf{T}\}_{n,n} x(n) + \sum_{m=0, m \neq n}^N \{\mathbf{T}\}_{n,m} x(m) + \{\mathbf{W}\mathbf{w}\}_n, \quad (21)$$

where  $n \in \{0, 1, \dots, N-1\}$ ,  $\mathbf{T} = \mathbf{W}\mathbf{H}_{\text{eff}}$ ,  $\{\cdot\}_{n,m}$  and  $\{\cdot\}_n$  represent the elements at corresponding positions in the matrix

or vector respectively. Therefore, the SINR on the  $n$ -th chirp-subcarrier is expressed as

$$\text{SINR}_n = \frac{|\{\mathbf{T}\}_{n,n}|^2}{\sum_{m=0, m \neq n}^{N-1} |\{\mathbf{T}\}_{n,m}|^2 + \sigma^2 \|\{\mathbf{W}\}_{n,:}\|^2} \quad (22)$$

where  $\{\cdot\}_{n,:}$  is the  $n$ -th row of the matrix.

### D. Effective SINR Loss

For the IDD channels, according to the I/O relationship of (17), the corresponding peak power of the  $i$ -th path is

$$P_{\text{IDD}} = |h_i|^2. \quad (23)$$

It can be seen that there is no SINR loss in this case.

For IDFD channels,  $|\mathcal{G}(m,n,k_{\nu_i},l_{\tau_i})|$  can be expressed as

$$|\mathcal{G}(m,n,k_{\nu_i},l_{\tau_i})| = \left| \frac{\sin(\pi(\psi - \kappa_{\nu_i}))}{N \sin(\frac{\pi(\psi - \kappa_{\nu_i})}{N})} \right|, \quad (24)$$

where  $\psi = [m - n + 2Nc_1l_{\tau_i} - \bar{k}_{\nu_i}]_N$  is integer. As mentioned before,  $|h_w(m,n,k_{\nu_i},l_{\tau_i})|$  has a peak at  $\psi = 0$ , i.e.,

$$|\mathcal{G}(m,n,k_{\nu_i},l_{\tau_i})| \leq \left| \frac{\sin(\pi\kappa_{\nu_i})}{N \sin(\frac{\pi\kappa_{\nu_i}}{N})} \right|. \quad (25)$$

Therefore, the corresponding peak power of the  $i$ -th path is

$$P_{\text{IDFD}} = |h_i|^2 \left| \frac{\sin(\pi\kappa_{\nu_i})}{N \sin(\frac{\pi\kappa_{\nu_i}}{N})} \right|^2. \quad (26)$$

Compared with (23), the SINR loss in the IDFD channels can be expressed as

$$L_{\text{SINR}}^{\text{IDFD}} = 20 \log_{10} \left| \frac{\sin(\pi\kappa_{\nu_i})}{N \sin(\frac{\pi\kappa_{\nu_i}}{N})} \right|^2 \approx 20 \log_{10} \left| \frac{\sin(\pi\kappa_{\nu_i})}{\pi\kappa_{\nu_i}} \right|^2, \quad (27)$$

where  $\pi\kappa_{\nu_i}/N$  approaches zero, resulting in  $\sin(\pi\kappa_{\nu_i}/N) \approx \pi\kappa_{\nu_i}/N$ .

For FDFD channels, similar to the previous derivation, the peak power corresponding to the  $i$ -th path is

$$P_{\text{FDFD}} = |h_i|^2 \left| \frac{\sin(\pi\gamma_i)}{N \sin(\frac{\pi\gamma_i}{N})} \right|^2. \quad (28)$$

Compared with (23), the SINR loss is

$$L_{\text{SINR}}^{\text{FDFD}} = 20 \log_{10} \left| \frac{\sin(\pi\gamma_i)}{N \sin(\frac{\pi\gamma_i}{N})} \right|^2 \approx 20 \log_{10} \left| \frac{\sin(\pi\gamma_i)}{\pi\gamma_i} \right|^2. \quad (29)$$

Fig. 2 shows the effective SINR loss for different fractional delays and fractional Dopplers at  $N = 64$ . The maximum SINR loss is about 7.843 dB. Moreover, according to (27) (29), increasing  $N$  cannot effectively reduce the SINR loss. In addition, since  $2Nc_1l_{\tau_i}$  can make the fractional part of the delay small enough, we can see that the  $\iota_{\tau_i}$  has almost no effect on SINR loss when  $\kappa_{\nu_i} = 0$ .

**Remark 1.** As shown in Fig. 2, the joint effects of fractional delay and fractional Doppler may result in a reduction of  $\gamma_i$  to alleviate the SINR loss.

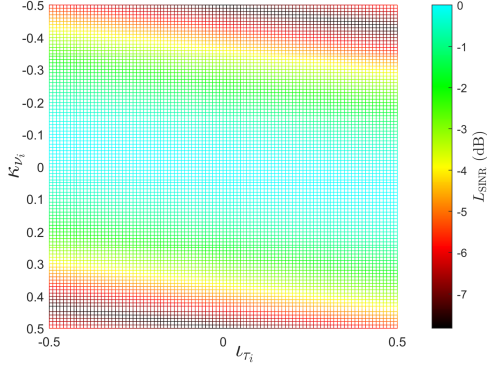


Fig. 2: Planform of SINR loss.

#### IV. MF AND MF-GFS CE SCHEMES FOR FDFD CHANNELS

In this section, we propose two low-complexity methods for estimating path parameters, by sequentially estimating the parameters of each individual path. Note that the chirp characteristic of separating different paths by  $c_1$  is leveraged in the proposed CE schemes. Due to the fact that the chirp characteristic is invalidated by  $c_1 = 0$  in OFDM systems, the method proposed cannot be directly applied to OFDM systems.

##### A. Problem Description

According to (12)-(15) and (64), the system model is

$$\mathbf{y} = \mathbf{A}(\mathbf{l}_\tau, \mathbf{k}_\nu) \mathbf{h} + \mathbf{w}, \quad (30)$$

where  $\mathbf{y} \in \mathbb{C}^{N \times 1}$  and  $\mathbf{w} \sim \mathcal{CN}(0, \sigma^2 \mathbf{I}_N) \in \mathbb{C}^{N \times 1}$  are vector forms of  $y(m)$  and  $w(m)$  respectively,  $\mathbf{I}_N$  is the  $N$ -order identity matrix, vectors  $\mathbf{l}_\tau = [l_{\tau_1}, \dots, l_{\tau_P}]^T \in \mathbb{R}^{P \times 1}$ ,  $\mathbf{k}_\nu = [k_{\nu_1}, \dots, k_{\nu_P}]^T \in \mathbb{R}^{P \times 1}$  and  $\mathbf{h} = [h_1, \dots, h_P]^T \in \mathbb{C}^{P \times 1}$  contain the normalized delay, normalized Doppler and channel gain, respectively.  $\mathbf{A}(\mathbf{l}_\tau, \mathbf{k}_\nu) \in \mathbb{C}^{N \times P}$  can be expressed as

$$\mathbf{A}(\mathbf{l}_\tau, \mathbf{k}_\nu) = [\mathbf{a}(l_{\tau_1}, k_{\nu_1}), \dots, \mathbf{a}(l_{\tau_P}, k_{\nu_P})], \quad (31)$$

where  $\mathbf{a}(l_{\tau_i}, k_{\nu_i}) \in \mathbb{C}^{N \times 1}$ , the  $m$ -th entry of  $\mathbf{a}(l_{\tau_i}, k_{\nu_i})$  is

$$\{\mathbf{a}(l_{\tau_i}, k_{\nu_i})\}_m = \sum_{n=0}^{N-1} x(n) \mathcal{G}(m, n, k_{\nu_i}, l_{\tau_i}), \quad (32)$$

where  $m \in \{0, \dots, N-1\}$ . It can be seen that  $\mathbf{A}(\mathbf{l}_\tau, \mathbf{k}_\nu)$  contains data, and channel information including  $k_{\nu_i}$ ,  $l_{\tau_i}$ ,  $P$ , which need to be estimated.

Pilots may be inserted into the DAFT domain for efficient CE. Due to the sparsity and compactness of the channel in the DAFT domain, a single pilot can be considered. The arrangement of pilot and data is shown in Fig. 3, which can be expressed as

$$x(n) = \begin{cases} x_p, & n = n_p \\ 0, & n_p - Q \leq n \leq n_p + Q, n \neq n_p \\ x_{\text{data}}, & \text{otherwise} \end{cases} \quad (33)$$

where  $x_p$  and  $x_{\text{data}}$  are single pilot and data, respectively,  $n_p$  is the pilot index in the DAFT domain grid,  $Q \triangleq (l_{\max} +$

$1)(2(k_{\max} + \xi) + 1) - 1$  due to the structure of  $\mathcal{G}(m, n, k_{\nu_i}, l_{\tau_i})$  and the analysis in Section III,  $Q_1 = k_{\max} + \xi$ ,  $Q_2 = Q - Q_1$ . The DAFT domain grid within the range  $n_p - Q \leq n \leq n_p + Q$ ,  $n \neq n_p$  remains null as a guard interval to reduce the mutual interference between data and pilot. The two types of guard intervals in Fig. 3 come from pilot and data, respectively.

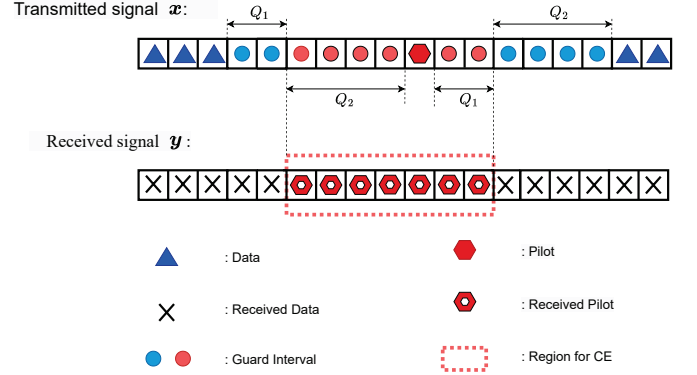


Fig. 3: Single pilot pattern for AFDM systems.

Based on the pilot pattern and the AFDM symbol structure in Fig. 3,  $y(m)$  in (12) is simplified to

$$y(m) = \sum_{i=1}^P h_i \mathcal{G}(m, n_p, k_{\nu_i}, l_{\tau_i}) x_p + z(n), \quad (34)$$

where  $n_p - Q_2 \leq m \leq n_p + Q_1$ ,  $z(n)$  is the new noise. The matrix form corresponding to (34) is

$$\mathbf{y}_T = \mathbf{x}_p \mathbf{A}_T(\mathbf{l}_\tau, \mathbf{k}_\nu) \mathbf{h} + \mathbf{z}_T, \quad (35)$$

where the subscript T indicates truncation, i.e.,  $n_p - Q_2 \leq m \leq n_p + Q_1$ . In the truncated  $\mathbf{A}_T(\mathbf{l}_\tau, \mathbf{k}_\nu) \in \mathbb{C}^{(Q+1) \times P}$ ,  $\mathbf{a}_T(l_{\tau_i}, k_{\nu_i}) \in \mathbb{C}^{(Q+1) \times 1}$  is given by

$$\{\mathbf{a}_T(l_{\tau_i}, k_{\nu_i})\}_m = \mathcal{G}(m, n_p, k_{\nu_i}, l_{\tau_i}). \quad (36)$$

##### B. Path Ambiguity in FDFD Channels

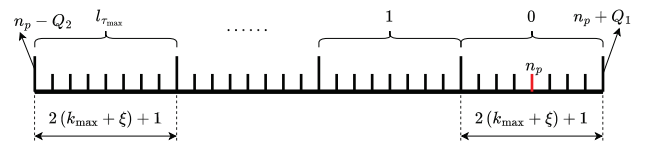


Fig. 4: Grid arrangement for IDD or IDFD channels.

For both IDD and IDFD channels, the integer parts of the parameters are estimated by

$$\hat{l}_{\tau_i} = \left\lfloor \frac{\hat{\gamma}_i}{-2Nc_1} \right\rfloor, \hat{k}_{\nu_i} = \hat{\gamma}_i + 2Nc_1 \hat{l}_{\tau_i}, \quad (37)$$

where  $\hat{\gamma}_i$  is the integer part of the estimated equivalent shift  $\hat{\chi}_i$ . That is, the integer delay-Doppler pair  $(\hat{l}_{\tau_i}, \hat{k}_{\nu_i})$  for a path uniquely corresponds to a position in the received signal  $\mathbf{y}_T$ . This correspondence can be seen in Fig. 4. However, in FDFD channels, (37) is invalid due to the fractional delay, thereby resulting in this one-to-one correspondence no longer holds.

For the FDFD channels, there are additional integer parts. First,  $2Nc_1\iota_{\tau_i}$  leads to a new integer part. In addition,  $-(2Nc_1\iota_{\tau_i} - \lfloor 2Nc_1\iota_{\tau_i} \rfloor) + \kappa_{\nu_i}$  yields another integer part and a final fractional part.

**Remark 2.** The extra integer parts may result in the inability to uniquely determine the delay and Doppler of a path. Such a phenomenon is referred to as path ambiguity, which involves delay ambiguity and Doppler ambiguity.

To simplify the explanation,  $-2Nc_1\iota_{\tau_i} + \bar{k}_{\nu_i} + \kappa_{\nu_i}$  can be regarded as an equivalent Doppler shift of a path, with the range of its integer part represented by

$$\mathcal{R}_\nu = \begin{cases} [-2k_{\max} - \xi - 1, k_{\max}], & \bar{l}_{\tau_i} = 0 \\ [-k_{\max}, 2k_{\max} + \xi + 1], & \bar{l}_{\tau_i} = l_{\max} \\ [-2k_{\max} - \xi - 1, 2k_{\max} + \xi + 1], & \text{otherwise} \end{cases} \quad (38)$$

However, the size of  $\mathcal{R}_\nu$  is significantly greater than  $2Nc_1$ . Therefore, the grids corresponding to each normalized delay overlap each other. This can be seen in Fig. 5.

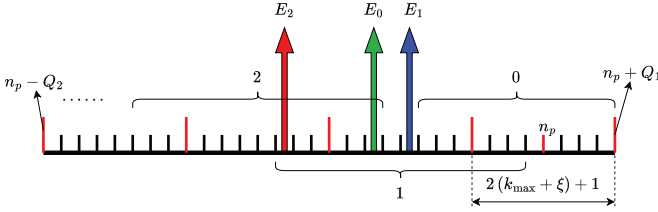


Fig. 5: Grid arrangement for FDFD channels.

This partial overlap will cause delay ambiguity and Doppler ambiguity. In Fig. 5, there are three arrows representing channel responses, i.e.,  $E_0$ ,  $E_1$ , and  $E_2$ . Assume that  $E_0$  corresponds to a path where  $l_{\tau_0} = \bar{l}_{\tau_0}$  and  $k_{\nu_0} = \bar{k}_{\nu_0} + \kappa_{\nu_0} < 0$ .  $E_1$  corresponds to a path where  $l_{\tau_1} = \bar{l}_{\tau_0} + \iota_{\tau_1}$  and  $k_{\nu_1} = k_{\nu_0}$ . If  $\iota_{\tau_1} < 0$ , we have  $-2Nc_1\iota_{\tau_1} > 0$ , causing  $E_1$  to move right relative to  $E_0$ . This leads to Doppler ambiguity. If  $-2Nc_1\iota_{\tau_1}$  is sufficiently large,  $E_1$  appears in the overlapping region of the grids corresponding to integer delays 1 and 0, resulting in simultaneous occurrence of both delay ambiguity and Doppler ambiguity.  $E_2$  corresponds to a path where  $l_{\tau_2} = \bar{l}_{\tau_0} + \iota_{\tau_2}$  and  $k_{\nu_2} = k_{\nu_0}$ . Similarly, if  $\iota_{\tau_2} > 0$ , both delay ambiguity and Doppler ambiguity will also exist simultaneously. Furthermore, due to the additional shift caused by fractional delay, even when an appropriate  $\xi$  is set, its ability to mitigate the ICCI between different paths is no longer effective. In addition,  $\xi$  may not eliminate path ambiguity. Unfortunately, there is no effective method to solve the path ambiguity problem.

### C. MF CE for FDFD channels

Assume that the wireless channel is a doubly-underspread channel [33], which remains static for a certain period of time. Specifically, the condition for the doubly-underspread channel is given by

$$\Delta\tau_{\max}\Delta\nu_{\max} \ll \tau_{\max}\nu_{\max} \ll 1, \quad (39)$$

where  $\Delta\tau_{\max} = \frac{\varpi}{c}$ ,  $\Delta\nu_{\max} = 2\nu_{\max} \sin(\frac{\varrho}{2})$ ,  $c$  is the speed of light, the maximum spatial extension and maximum angular

Transmitted signal:

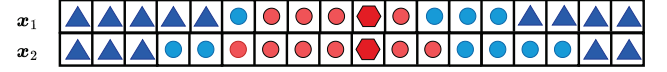


Fig. 6: The proposed pilot pattern in FDFD channel for AFDM systems.

spread of the scatterers are assumed to be  $\varpi = 30$  m and  $\varrho = \frac{\pi}{60}$ , respectively. Considering the simulation parameters in Table II of Section VI, we have  $\Delta\tau_{\max}\Delta\nu_{\max} = 1.0471 \times 10^{-5} \ll \tau_{\max}\nu_{\max} = 3.12 \times 10^{-2} \ll 1$ . Therefore, the channel considered is doubly-underspread. Based on  $T$  and the stationary time  $\frac{1}{\Delta\nu_{\max}}$ , the number of AFDM symbols during the stationary time of the channel is 9.

Therefore, considering the doubly-underspread channel, two AFDM symbols can be used for CE. The key idea is to use the different equivalent shifts of a path in the two AFDM symbols to uniquely determine the delay and Doppler. In addition, the new pilot pattern<sup>3</sup> in Fig. 6 is proposed to estimate equivalent shifts, where both  $x_1$  and  $x_2$  have the structure shown in Fig. 3. In addition, for  $x_1$ , the truncated received signal is  $y_T$ ,  $c_1$  is determined by  $\xi$  in (2). For  $x_2$ , similarly,  $y'_T$ ,  $c'_1$ , and  $\xi'$  can be defined. Note that setting  $\xi \neq \xi'$  leads to  $c_1 \neq c'_1$ , thereby resulting in different equivalent shifts.

For the estimation of equivalent shift, let us consider  $x_1$  as an example. Based on (35), the joint maximum likelihood estimation (JMLE) of  $(l_\tau, k_\nu, h)$  can be expressed as

$$(\hat{l}_\tau, \hat{k}_\nu, \hat{h}) = \arg \min_{(l_\tau, k_\nu, h)} \|y_T - x_p A_T(l_\tau, k_\nu) h\|^2. \quad (40)$$

According to [34],  $(\hat{l}_\tau, \hat{k}_\nu)$  can be expressed as (41), as shown at the bottom of next page,  $\hat{h}$  is given by

$$\hat{h} = \frac{1}{x_p} \left( A_T^H(\hat{l}_\tau, \hat{k}_\nu) A_T(\hat{l}_\tau, \hat{k}_\nu) \right)^{-1} A_T^H(\hat{l}_\tau, \hat{k}_\nu) y_T. \quad (42)$$

**Theorem 2.** Different columns in  $A_T(l_\tau, k_\nu)$  can be approximately orthogonal, making  $A_T^H(l_\tau, k_\nu) A_T(l_\tau, k_\nu)$  close enough to the identity matrix. In addition, the larger the  $N$  or  $\xi$ , the better the orthogonality.

*Proof:* The proof is given in Appendix B. ■

Thus, based on the orthogonality, (41) and (42) can be well approximated as

$$(\hat{l}_\tau, \hat{k}_\nu) \approx \arg \max_{(l_\tau, k_\nu)} \sum_{i=1}^P |a_T^H(l_{\tau_i}, k_{\nu_i}) y_T|^2. \quad (43)$$

$$\hat{h} \approx \frac{A_T^H(\hat{l}_\tau, \hat{k}_\nu) y_T}{x_p}. \quad (44)$$

Since  $a_T(l_{\tau_i}, k_{\nu_i})$  and  $a_T(l_{\tau_j}, k_{\nu_j})$  are approximately orthogonal, they exhibit path separability, where  $i \neq j$ . The separability of the two paths improves as  $N$  increases. In addition,  $y_T = \sum_{i=1}^P x_p h_i a_T(l_{\tau_i}, k_{\nu_i})$ . Therefore,  $(h_i, l_{\tau_i}, k_{\nu_i})$  of each path can be estimated separately.

<sup>3</sup>An alternative pilot pattern, where  $x_1$  and  $x_2$  have identical waveform parameters except for  $N$ , can also achieve the same purpose.



Therefore, based on the separability of the channel in the DAFT domain, the joint estimation of parameters for all paths can be decoupled. The estimation result for the  $i$ -th path is

$$\left(\hat{l}_{\tau_i}, \hat{k}_{\nu_i}\right) \approx \arg \max_{(l_{\tau}, k_{\nu})} \left| \mathbf{a}_T^H(l_{\tau}, k_{\nu}) \mathbf{y}_T \right|^2, \quad (45)$$

$$\hat{h}_i \approx \frac{1}{x_p} \mathbf{a}_T^H\left(\hat{l}_{\tau_i}, \hat{k}_{\nu_i}\right) \mathbf{y}_T. \quad (46)$$

Due to the path ambiguity,  $\left(\hat{l}_{\tau_i}, \hat{k}_{\nu_i}\right)$  in (45) cannot be estimated accurately. However, the estimation of equivalent shift  $\chi_i = \gamma_i + \gamma_i = -2Nc_1 l_{\tau_i} + \frac{\nu_i}{\Delta f}$  is not affected. Therefore, (45) can be reformulated as

$$\hat{\chi}_i \approx \arg \max_{\chi_i} \left| \mathcal{T}^H(\chi) \mathbf{y}_T \right|^2, \quad (47)$$

where  $\{\mathcal{T}(\chi)\}_m = \mathcal{J}(m, n_p, \chi_i)$ ,  $n_p - Q_2 \leq m \leq n_p + Q_1$ ,  $\mathcal{J}(m, n_p, \chi_i)$  is defined in (19).

For (47),  $\hat{\chi}_i$  can be obtained by searching for consecutive  $\chi$ . Specifically, since  $\mathbf{a}_T(l_{\tau_i}, k_{\nu_i})$  in  $\mathbf{y}_T$  and  $\mathcal{T}(\chi)$  have the same structure, it can be anticipated that  $\left| \mathcal{T}^H(\chi) \mathbf{y}_T \right|$  will achieve its maximum value at  $\chi = \chi_i$ . This proof is similar to Appendix C. However, the complexity of searching for  $\hat{\chi}_i$  is still high. A simple and effective method is to estimate  $\hat{\gamma}_i$  using the index  $n_{\text{peak}}$  of the maximum peaks in  $\mathbf{y}_T$ , i.e.,

$$\hat{\gamma}_i = n_{\text{peak}} - n_p, \quad (48)$$

the fractional  $\hat{\gamma}_i$  can be obtained by searching within a small range  $[-0.5, 0.5]$ . For  $\hat{\gamma}_i$ , the continuous range  $[-0.5, 0.5]$  can first be uniformly discretized into a grid  $\mathbf{F} \in \mathbb{R}^{(\rho+1) \times 1}$ , i.e.,

$$\{\mathbf{F}\}_{\tilde{n}} = -0.5 + \frac{1}{\rho} \tilde{n}, \tilde{n} \in [0, \rho], \quad (49)$$

where  $\rho$  is the size of the search step. Thus,  $\hat{\gamma}_i$  is given by

$$\hat{\gamma}_i = \arg \max_{\gamma \in \mathbf{F}} \left| \mathcal{T}^H\left(\hat{\gamma}_i + \gamma\right) \mathbf{y}_T \right|^2. \quad (50)$$

For  $x_2$ , the equivalent shift  $\chi'_i = \gamma'_i + \gamma'_i = -2Nc'_1 l_{\tau_i} + \frac{\nu_i}{\Delta f}$  of the  $i$ -th path can also be estimated using the above method. Based on the estimated  $\hat{\chi}_i$  and  $\hat{\chi}'_i$ ,  $\left(\hat{l}_{\tau_i}, \hat{k}_{\nu_i}\right)$  can be given by

$$\hat{l}_{\tau_i} = \frac{\hat{\chi}'_i - \hat{\chi}_i}{2N(c_1 - c'_1)}, \quad (51)$$

$$\hat{k}_{\nu_i} = \frac{\hat{\nu}_i}{\Delta f} = \hat{\chi}_i + 2Nc_1 \hat{l}_{\tau_i}. \quad (52)$$

Noted that  $\left(\hat{h}_i, \hat{l}_{\tau_i}, \hat{k}_{\nu_i}\right)$  in (46), (48)-(52) represent the estimation results for single path. For multiple paths, an iterative estimation scheme is required. Specifically, the signal corresponding to  $\left(\hat{l}_{\tau}^{(t)}, \hat{k}_{\nu}^{(t)}, \hat{h}^{(t)}\right)$  in the  $(t)$ -th iteration is

$$\mathbf{y}_T^{(t),t} = x_p \hat{h}^{(t)} \mathbf{a}\left(\hat{l}_{\tau}^{(t)}, \hat{k}_{\nu}^{(t)}\right) \in \mathbb{C}^{(Q+1) \times 1}. \quad (53)$$

---

**Algorithm 1** Proposed MF CE scheme for FDFD channels

---

**Input:** Received signal  $\mathbf{y}_T$  and  $\mathbf{y}'_T$ .

**Initialization:**  $\mathbf{y}'_T^{(t)} = \mathbf{y}'_T$ ,  $\mathbf{y}_T^{(t)} = \mathbf{y}_T$ , the maximum number of iterations  $T_{\text{iter}}$ , threshold  $\sigma$ ,  $l_{\text{max}}$ ,  $k_{\text{max}}$ ,  $\hat{l}_{\tau} = \emptyset$ ,  $\hat{k}_{\nu} = \emptyset$ ,  $\hat{h} = \emptyset$ ,  $t = 1$ .

1: **repeat**

2: According to (48),  $\hat{\gamma}_i$  and  $\hat{\gamma}'_i$  are obtained.

3: According to (50),  $\hat{\gamma}_i$  and  $\hat{\gamma}'_i$  are estimated.

4: According to (51) and (52),  $\hat{l}_{\tau}^{(t)}$  and  $\hat{k}_{\nu}^{(t)}$  are obtained.

5:  $\hat{h}^{(t)}$  can be obtained by (46).

6:  $\hat{l}_{\tau} = \left[\hat{l}_{\tau}, \hat{l}_{\tau}^{(t)}\right]$ ,  $\hat{k}_{\nu} = \left[\hat{k}_{\nu}, \hat{k}_{\nu}^{(t)}\right]$ ,  $\hat{h} = \left[\hat{h}, \hat{h}^{(t)}\right]$ .

7: The  $\mathbf{y}_{T_1}^{(t+1)}$  and  $\mathbf{y}_{T_2}^{(t+1)}$  are obtained by (54).

8:  $t = t + 1$ .

9: until  $t = T_{\text{iter}}$  or  $\left\| \frac{\mathbf{y}_T^{(t+1)} - \mathbf{y}_T^{(t)}}{\mathbf{y}_T^{(t)}} \right\| \leq \sigma$ .

**Output:**  $\left(\hat{l}_{\tau}, \hat{k}_{\nu}, \hat{h}\right)$ .

---

Before estimating the next path,  $\mathbf{y}_T^{(t),t}$  is subtracted from the received signal  $\mathbf{y}_T^{(t)}$ , i.e.,

$$\mathbf{y}_T^{(t+1)} = \mathbf{y}_T^{(t)} - \mathbf{y}_T^{(t),t}. \quad (54)$$

For  $\mathbf{y}'_T$ , the same process is performed. The iteration terminates if the maximum number  $T_{\text{iter}}$  is reached or  $\left\| \frac{\mathbf{y}_T^{(t+1)} - \mathbf{y}_T^{(t)}}{\mathbf{y}_T^{(t)}} \right\| / \left\| \mathbf{y}_T^{(t)} \right\| \leq \sigma$ , where the preset threshold  $\sigma > 0$ . The MF CE scheme is summarized in **Algorithm 1**.

#### D. MF-GFS CE for FDFD channels

In Subsection IV-C, an MF-based CE scheme is proposed. This scheme eliminates the matrix inversion operation, decouples joint estimation, and narrows the search range to significantly reduce the computational complexity. However, the trade-off between the complexity and estimation performance of the MF CE scheme yet depends on the  $\rho$  in (49). The larger the  $\rho$ , the finer the grid  $\mathbf{F}$ , enabling more accurate estimation of fractional part. In this case,  $\left(\hat{l}_{\tau}, \hat{k}_{\nu}, \hat{h}\right)$  will become more accurate. However, the cost of increasing  $\rho$  is that the complexity will inevitably increase. To address this issue, we introduce a MF-GFS CE scheme based on the GFS algorithm in this subsection, by significantly reducing the search range of fractional part to reduce complexity and estimating  $\left(\hat{l}_{\tau}, \hat{k}_{\nu}, \hat{h}\right)$  more accurately.

GFS is an unconstrained nonlinear optimization method for unimodal functions [35]–[37]. The GFS algorithm unevenly divides the search interval into two parts through the ratio of two consecutive generalized Fibonacci numbers (GFNs) to achieve an efficient search. The  $i$ -th GFN is denoted by  $S_i(a, b, p, q)$ , where  $i$  is a non-negative integer. Note that the conditions that must be satisfied to estimate the optimal value of a function using the GFS algorithm are:

---


$$\left(\hat{l}_{\tau}, \hat{k}_{\nu}\right) = \arg \max_{(l_{\tau}, k_{\nu})} \mathbf{y}_T^H \mathbf{A}_T(l_{\tau}, k_{\nu}) \left( \mathbf{A}_T^H(l_{\tau}, k_{\nu}) \mathbf{A}_T(l_{\tau}, k_{\nu}) \right)^{-1} \mathbf{A}_T^H(l_{\tau}, k_{\nu}) \mathbf{y}_T. \quad (41)$$

- $a + b > 0$ , and  $p$  as well as  $q$  are two positive integers.
- The function to be optimized needs to be a bounded unimodal function.

**Theorem 3.** In (50), the objective function  $\left| \mathcal{T}^H (\hat{\gamma}_i + \gamma) \mathbf{y}_T \right|^2$  is a bounded unimodal function.

*Proof:* The proof is given in Appendix C. ■

After dividing the search interval by two consecutive GFNs, the interval of uncertainty (IU) containing the optimal value  $\gamma_i$  needs to be determined. For convenience, assume that the search interval is  $[x_s, x_f]$ , and  $x_s < x_1 < x_2 < x_f$ . The new IU  $[x'_s, x'_f]$  can be expressed as

$$[x'_s, x'_f] = \begin{cases} [x_s, x_2], & f(x_1) < f(x_2) \\ [x_1, x_f], & f(x_1) > f(x_2) \end{cases}. \quad (55)$$

Note that  $|x'_f - x'_s| < |x_f - x_s|$ .

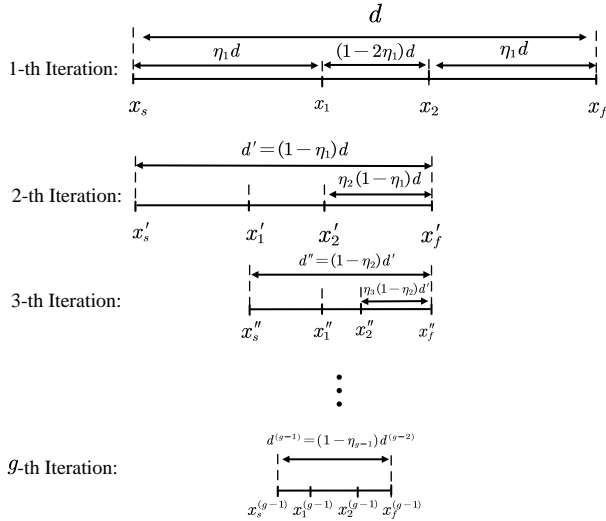


Fig. 7: The diagram of the GFS algorithm.

The process of the GFS algorithm for estimating  $\hat{\gamma}_i$  is shown in Fig. 7. Note that it is necessary to set a maximum GFN  $S_{N_G}(a, b, p, q)$ ,  $N_G = T_G + 2$ , which determines the maximum number of iterations,  $T_G$ , for the GFS. For the  $g$ -th iteration, the IU is divided based on the ratio of two successive higher GFNs, i.e.,

$$\eta_g = \frac{qS_{N_G-(g+1)}(a, b, p, q)}{S_{N_G-(g-1)}(a, b, p, q)}, \quad (56)$$

where  $g \in [1, T_G]$ .  $\eta_g$  can determine the positions of  $x_1^{(g-1)}$  and  $x_2^{(g-1)}$ . In general, for the  $g$ -th iteration, the size of IU is

$$d^{(g-1)} = (1 - \eta_{g-1}) d^{(g-2)}. \quad (57)$$

Then, the new IU can be obtained by (55). The iteration will terminate if the maximum number  $T_G$  is reached or

$$d^{(g-1)} = |x_f^{(g-1)} - x_s^{(g-1)}| < \varepsilon, \quad (58)$$

where  $\varepsilon$  is the pre-set threshold. At this moment, if there is no additional prior, fractional part can be estimated as

$$\hat{\gamma}_i = \frac{x_s^{(g-1)} + x_f^{(g-1)}}{2}, \quad (59)$$

## Algorithm 2 GFS Algorithm

**Input:** Received signal  $\mathbf{y}_T$

**Initialization:**  $g = 1$ ,  $x_s^{(0)} = -0.5$ ,  $x_f^{(0)} = 0.5$ , the objective function  $f(\gamma) = \left| \mathcal{T}^H (\hat{\gamma}_i + \gamma) \mathbf{y}_T \right|^2$ .

1: **repeat**

2: From (57) and (56),  $x_1^{(g-1)}$  and  $x_2^{(g-1)}$  are obtained.

3: According to (55), the new IU is obtained.

4:  $g = g + 1$ .

5: **until**  $g = T_G$  or  $d^{(g-1)} = |x_f^{(g-1)} - x_s^{(g-1)}| < \varepsilon$ .

6: Calculate  $\hat{\gamma}_i$  according to (59).

**Output:**  $\hat{\gamma}_i$ .

## Algorithm 3 The proposed MF-GFS CE scheme for IDFD channels

**Input:** Received signal  $\mathbf{y}_T$ .

**Initialization:**  $\mathbf{y}_T^{(t)} = \mathbf{y}_T$ , the maximum number of iterations  $T_{\text{iter}}$  and  $T_G$ , threshold  $\sigma$  and  $\varepsilon$ ,  $l_{\text{max}}$ ,  $k_{\text{max}}$ ,  $\hat{l}_\tau = \emptyset$ ,  $\hat{k}_\nu = \emptyset$ ,  $\hat{h} = \emptyset$ ,  $t_{\text{iter}} = 1$ .

1: **repeat**

2: According to (60),  $(\hat{l}_\tau^{(t)}, \hat{k}_\nu^{(t)})$  for a path is obtained.

3: Based on (61), estimate  $\hat{\kappa}_\nu^{(t)}$  by **Algorithm 2**.

4:  $\hat{h}^{(t)}$  can be obtained by (46).

5:  $\hat{l}_\tau = [\hat{l}_\tau, \hat{l}_\tau^{(t)}]$ ,  $\hat{k}_\nu = [\hat{k}_\nu, \hat{k}_\nu^{(t)}]$ ,  $\hat{h} = [\hat{h}, \hat{h}^{(t)}]$ .

6:  $\mathbf{y}_T^{(t+1)}$  is obtained by (54).

7:  $t = t + 1$ .

8: **until**  $t = T_{\text{iter}}$  or  $\left\| \frac{\mathbf{y}_T^{(t+1)} - \mathbf{y}_T^{(t)}}{\mathbf{y}_T^{(t)}} \right\| \leq \sigma$ .

**Output:**  $(\hat{l}_\tau, \hat{k}_\nu, \hat{h})$ .

The GFS algorithm for estimating  $\hat{\gamma}_i$  is summarized in **Algorithm 2**. Except for  $\hat{\gamma}_i$ , the MF-GFS scheme follows the same procedure as the MF scheme. For the MF-GFS scheme,  $\hat{\gamma}_i$  is obtained via the **Algorithm 2** rather than (50).

Note that the size of IU in the MF scheme is  $\frac{1}{\rho+1}$ , which is generally on the magnitude of  $10^{-1}$  or  $10^{-2}$ . However, the size of IU in the MF-GFS scheme is several orders of magnitude smaller. Therefore, the proposed MF-GFS scheme is generally more effective than the MF scheme.

## E. MF-GFS CE scheme for IDFD channels

In typical wide-band systems such as satellite communications or millimeter-wave communications,  $B$  is sufficiently large to approximate  $\tau_i$  to the nearest sampling point [7], [38]. Therefore, an MF-GFS scheme is proposed for IDFD channels.

The observation model in (35) is still considered. The estimation of  $(h_i, l_{\tau_i} = \bar{l}_{\tau_i}, k_{\nu_i} = \bar{k}_{\nu_i} + \kappa_{\nu_i})$  for the  $i$ -th path can also be expressed as (45) and (46). Since the  $\iota_{\tau_i} = 0$ , path ambiguity does not exist. Therefore, based on the pilot pattern in Fig. 3,  $(\hat{l}_{\tau_i}, \hat{k}_{\nu_i})$  can be accurately estimated.

For (45),  $(\hat{l}_{\tau_i}, \hat{k}_{\nu_i})$  can be obtained by searching for consecutive  $(l_{\tau_i}, k_{\nu_i})$ . It can be anticipated that  $|\mathbf{a}_T^H(l_{\tau_i}, k_{\nu_i}) \mathbf{y}_T|$  achieves its maximum value at  $(l_{\tau_i}, k_{\nu_i}) = (l_{\tau_i}, k_{\nu_i})$ . However, the complexity of searching for  $(\hat{l}_{\tau_i}, \hat{k}_{\nu_i})$  in space



$\{[0, l_{\max}] \times [-k_{\max}, k_{\max}]\}$  is still high. A simple and effective method is to estimate  $(\hat{l}_{\tau_i}, \hat{k}_{\nu_i})$  of the path based on the maximum peaks in the received signal  $\mathbf{y}_T$ , i.e.,

$$(\hat{l}_{\tau_i}, \hat{k}_{\nu_i}) \leftarrow m_{\max} = \underset{m}{\operatorname{argmax}} |\{\mathbf{y}_T\}_m|. \quad (60)$$

The estimation of  $\kappa_{\nu_i}$  can be expressed as

$$\hat{\kappa}_{\nu_i} = \arg \max_{\kappa_{\nu} \in \Gamma} \left| \mathbf{a}_T^H(\hat{l}_{\tau_i}, \hat{k}_{\nu_i} + \kappa_{\nu}) \mathbf{y}_T \right|^2. \quad (61)$$

The MF scheme is to directly search the grid  $\Gamma$  to get  $\hat{\kappa}_{\nu_i}$ . In addition,  $\left| \mathbf{a}_T^H(\hat{l}_{\tau_i}, \hat{k}_{\nu_i} + \kappa_{\nu}) \mathbf{y}_T \right|^2$  is a bounded unimodal function, achieving its extreme value at  $\kappa_{\nu} = \kappa_{\nu_i}$ . This proof is similar to that of **Theorem 3**. Therefore, to reduce redundant computation and improve performance, **Algorithm 2** is used to estimate  $\hat{\kappa}_{\nu_i}$ . Note that the same iterative method is also considered for parameter estimation of multiple paths, which estimates one path in one iteration. The proposed MF-GFS CE scheme for IDFD channels is summarized in **Algorithm 3**.

### F. Complexity Analysis

In this subsection, we analyze complexity of the proposed MF and MF-GFS CE schemes. For the MF CE in the IDFD channels, The complexity of (60) is  $\mathcal{O}(Q)$ . In addition, based on (61), estimating  $\hat{\kappa}_{\nu_i}$  requires  $\mathcal{O}(Q\rho)$ . Calculating (46) costs  $\mathcal{O}(Q)$ . To calculate  $\mathbf{y}_T^{(t+1)}$  in (54),  $\mathcal{O}(Q)$  are required. Therefore, the complexity in each iteration is  $\mathcal{O}(Q\rho)$ . For the proposed MF-GFS CE scheme in the IDFD channel, estimating  $\hat{\kappa}_{\nu_i}$  through **Algorithm 2** costs  $\mathcal{O}(T_G Q)$ . Therefore, the complexity in each iteration is  $\mathcal{O}(T_G Q)$ . The remaining analysis is similar to the MF scheme. The complexity is summarized in Table I, where  $L$  is the number of columns in the measurement matrix for the CS schemes. Fig. 8 is the complexity comparison, where  $l_{\max} = 8$ ,  $k_{\max} \in [2, 10]$ . one can see the low-complexity nature of the proposed schemes.

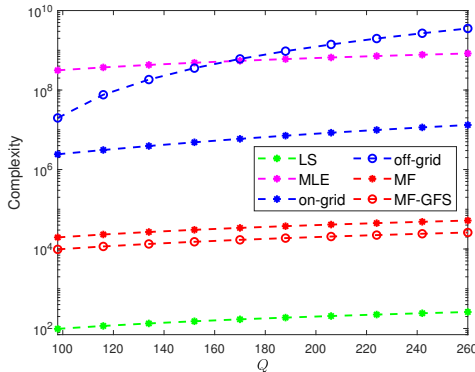


Fig. 8: Complexity comparison of different CE schemes.

## V. SIMULATION RESULTS

In this section, the CE performances of the proposed MF and MF-GFS methods are evaluated. Unless otherwise stated, the simulation parameters are shown in Table II.  $\tau_i$  and  $\nu_i$  are randomly and uniformly generated within  $[0, \tau_{\max}]$  and

$[-\nu_{\max}, \nu_{\max}]$ , respectively. The system signal-to-noise ratio (SNR) is defined as  $\frac{E\{|x(n)|^2\}}{\sigma^2}$ , where  $E\{\cdot\}$  is the expected operation. For the pilot  $x_p$ ,  $10 \log_{10} \frac{|x_p|^2}{E\{|x(n)|^2\}} = 30$  dB is satisfied. For the proposed algorithms, set  $T_{\text{iter}} = 15$ ,  $\sigma = 10^{-3}$ ,  $\rho = 20$ . For comparison, we consider the traditional LS scheme [28], the MLE scheme [15], the on-grid scheme [29], [30] with OMP algorithm, and the off-grid scheme [31]. For CE schemes based on CS algorithm, the grid resolution is 0.5. We reconstruct  $\hat{\mathbf{H}}_{\text{eff}}$  using the estimated parameters, and define NMSE as  $\text{NMSE} = \|\mathbf{H}_{\text{eff}} - \hat{\mathbf{H}}_{\text{eff}}\|^2 / \|\mathbf{H}_{\text{eff}}\|^2$ .

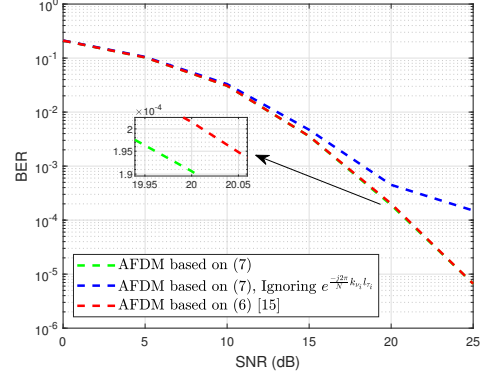


Fig. 9: Comparison of different AFDM frameworks.

Fig. 9 shows the BER performance comparison for different AFDM frameworks, whereby the BER is obtained by LMMSE algorithm. The performances of the two AFDM frameworks are consistent. In addition, if the coupling phase  $e^{-j\frac{2\pi}{N}k_{\nu_i}l_{\tau_i}}$  is not considered, the BER will be severely deteriorated.

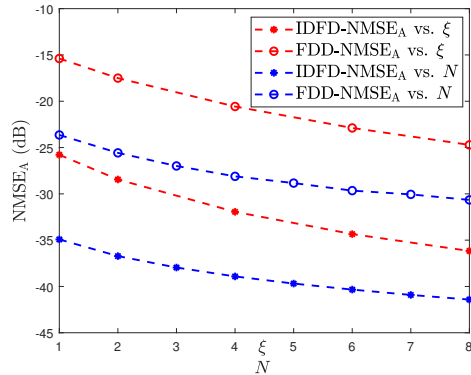


Fig. 10: Orthogonality of  $\mathbf{A}_T(l_{\tau}, \mathbf{k}_{\nu})$  vs.  $\xi$  and  $N$ .

The approximate orthogonality of  $\mathbf{A}_T(l_{\tau}, \mathbf{k}_{\nu})$  for different values of  $\xi$  and  $N$  is shown in Fig. (10). For “NMSE<sub>A</sub> vs.  $\xi$ ”, we consider  $N = 256$ ,  $\xi \in [1, 8]$ . For “NMSE<sub>A</sub> vs.  $N$ ”, we have  $\xi = 4$ ,  $N \in 200 \times [1, 8]$ . To make this orthogonality more obvious, the integer parts of the delays for different paths are set to differ. Note that  $\text{NMSE}_A = \|\mathbf{I} - \mathbf{A}_T^H(l_{\tau}, \mathbf{k}_{\nu}) \mathbf{A}_T(l_{\tau}, \mathbf{k}_{\nu})\|^2 / \|\mathbf{I}\|^2$ . It can be observed that this approximate orthogonality is still good enough even in fractional channels. This orthogonality improves with the increase of  $\xi$  or  $N$  in both IDFD and FDD channels, which is also confirmed in Appendix B.

TABLE I: COMPARISON OF COMPLEXITY

Method	Complexity
LS scheme [28]	$\mathcal{O}(Q)$
MLE scheme [15]	$\mathcal{O}(\rho^P Q)$
on-grid scheme [29], [30]	$\mathcal{O}(T_{\text{iter}}^3 + T_{\text{iter}} L Q + T_{\text{iter}}^2 Q)$
off-grid scheme [31]	$\mathcal{O}(T_{\text{iter}} L^2 Q)$
The proposed MF scheme for IDFD channels	$\mathcal{O}(T_{\text{iter}} \rho Q)$
The proposed MF-GFS scheme for IDFD channels	$\mathcal{O}(T_{\text{iter}} T_G Q)$
The proposed MF scheme for FDFD channels	$\mathcal{O}(T_{\text{iter}} \rho Q)$
The proposed MF-GFS scheme for FDFD channels	$\mathcal{O}(T_{\text{iter}} T_G Q)$

TABLE II: SIMULATION PARAMETERS

Parameter	Value
The number of chirp-carriers	$N = 256$
Carrier frequency	4 GHz
The channel coefficient	$h_i \sim \mathcal{CN}(0, \frac{1}{P})$
Maximum delay	$\tau_{\text{max}} = 1.56 \times 10^{-5} \text{s}$
Maximum relative velocity	540 km/h
Maximum Doppler shift	$2 \times 10^3 \text{ Hz}$
Subcarrier spacing	$\Delta f = 1 \text{ kHz}$
Number of channel paths	$P = 5$
Data modulation	4-QAM
$\xi, \xi'$	4, 5

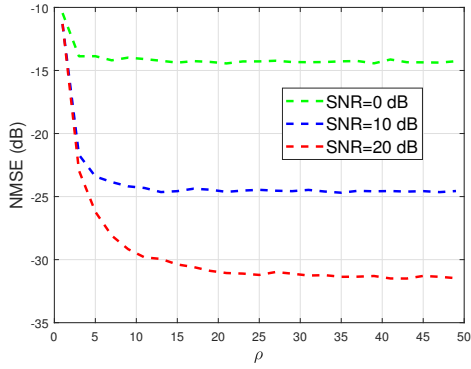
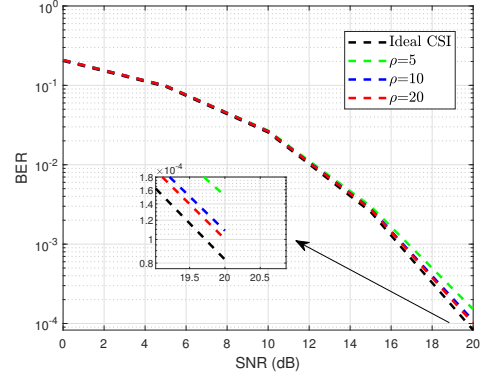
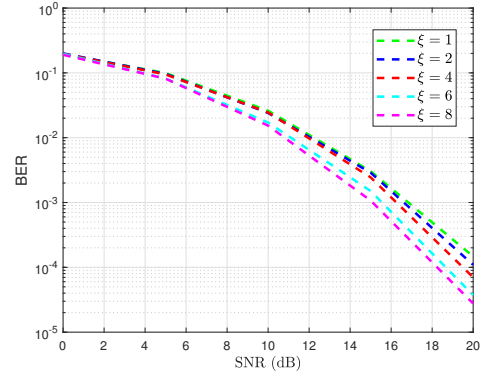
Fig. 11: NMSE comparison of the proposed MF scheme versus  $\rho$  for different SNR values.

Fig. 11 and 12 show the NMSE and BER performances of the proposed MF scheme for IDFD channel with different SNR and  $\rho$ , respectively. As  $\rho$  increases, the size of IU correspondingly decreases, enabling more accurate estimation of the fractional Doppler, which leads to improvements in both NMSE and BER.

The impact of different  $\xi$  on the BER performance of the MF scheme is shown in Fig. 13. It can be observed that the BER performance improves as the  $\xi$  increases. In this case, the interference between different paths will decrease, making the estimated parameters more accurate, and hence improved BER performance. In addition, according to Appendix B and Fig. 10, as  $\xi$  increases, the orthogonality performance of  $\mathbf{A}_T(\mathbf{l}_\tau, \mathbf{k}_\nu)$  is improved, thus leading to further improved CE and BER performances.

The NMSE and BER performances of different schemes for IDFD channels are compared in Fig. 14 and Fig. 15, respectively. We set  $\rho = 10$  and  $N_G = 15$  to allow a comparison of the MF scheme and the MF-GFS scheme at almost the same complexity levels. In addition, the performance of the MF-GFS

Fig. 12: BER comparison of the proposed MF scheme versus SNR for different  $\rho$  values.Fig. 13: BER comparison of the proposed MF scheme versus SNR for different  $\xi$  values.

scheme with different GFN, distinguished by  $(a, b, p, q)$ , is also compared. It can be observed that the performance of the proposed MF scheme and MF-GFS scheme are significantly improved compared to that of other schemes. Since the size of the IU estimated by the MF-GFS scheme is significantly smaller than that of MF, it can be seen that the performance of the proposed MF-GFS scheme outperforms that of the MF scheme at high SNR. In addition, since the ratio of two consecutive GFNs is generally close to the golden ratio, different GFNs yield similar IU divisions, thereby resulting in a negligible impact on the performance of the MF-GFS scheme.

Fig. 16 is a comparison of BER performance for FDFD channels. For simple verification, assume that the relative

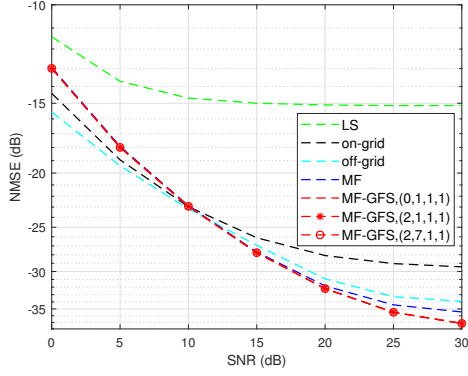


Fig. 14: Comparison of NMSE performance.

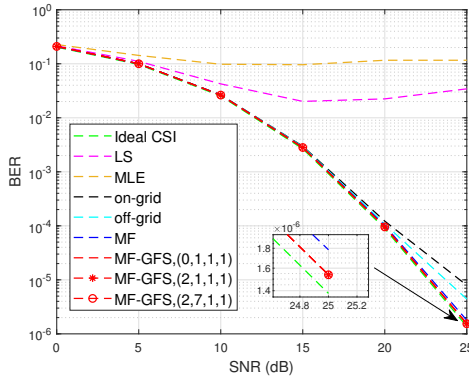


Fig. 15: Comparison of BER performance.

positions of the peaks of the pilot responses in  $\mathbf{y}_{T_1}$  and  $\mathbf{y}_{T_2}$  are known. Since the LS, MLE, on-grid and off-grid schemes fail to address the path ambiguity caused by fractional delay, they suffer from poor BER performance. In contrast, the proposed MF and MF-GFS schemes outperform significantly as they can achieve accurate estimation in FDFD channels.

## VI. CONCLUSIONS

This paper has studied an MF-based CE scheme for AFDM systems over doubly selective channels, by upholding the key idea of sequentially estimating the parameters of each path. We have derived the I/O relationship of AFDM and analyzed the ICCI, SINR and effective SINR loss for different channels.

We have also studied the path ambiguity problem for FDFD channels that causes severe performance deterioration. To address such a path ambiguity problem, we have introduced a novel pilot pattern across two AFDM transmissions, followed by an MF CE scheme. Specifically, by leveraging the orthogonality and separability between different paths, we have shown that the multipath estimation can be decoupled into low-complexity estimations for individual paths. Consequently, the equivalent shift of each path can be estimated sequentially. In addition, different equivalent shifts corresponding to a path are employed to solve the path ambiguity problem.

To further reduce the search space and redundant computation during fractional parameter estimation, we have proposed the MF-GFS CE scheme that outperforms the proposed MF.

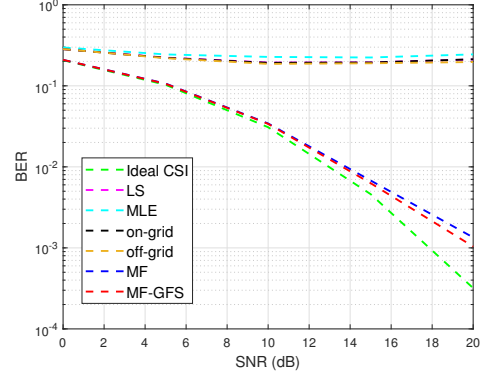


Fig. 16: Comparison of BER performance for FDFD channels.

We have also extended the proposed MF and MF-GFS CE schemes to the typical broadband systems. The simulation results have shown that the proposed schemes offer more significant advantages over existing CE schemes in terms of improved communication performances and lower complexities.

## APPENDIX A

### PROOF OF THEOREM 1: I/O RELATION OF AFDM IN DAFT DOMAIN

To analyze the impact of each path, a more detailed I/O relationship is required. Substituting (1), (8) and the DAFT kernel  $F_{c_1, c_2}(\cdot)$  into (10),  $y(m)$  can be expressed as (65). Combining all complex exponential terms yields (66). By grouping the terms involving  $\bar{n}$  together,  $y(m)$  can be expressed as

$$y(m) = \sum_{n=0}^{N-1} x(n) h_w(m, n) + w(n), \quad (62)$$

where  $h_w(m, n)$  is given by (67) at the top of next page, with

$$\alpha(m, n, k_{\nu_i}, l_{\tau_i}) = e^{-\frac{j2\pi}{N}(-Nc_1 l_{\tau_i}^2 + (n + k_{\nu_i})l_{\tau_i} + Nc_2(m^2 - n^2))}, \quad (63)$$

$$\begin{aligned} \mathcal{F}(m, n, k_{\nu_i}, l_{\tau_i}) &= \frac{1}{N} \sum_{\bar{n}=0}^{N-1} e^{-\frac{j2\pi}{N}(m-n+2Nc_1 l_{\tau_i} - k_{\nu_i})\bar{n}} \\ &= \frac{1}{N} \frac{e^{-j2\pi(m-n+2Nc_1 l_{\tau_i} - k_{\nu_i})} - 1}{e^{-j\frac{2\pi}{N}(m-n+2Nc_1 l_{\tau_i} - k_{\nu_i})} - 1} \end{aligned} \quad (64)$$

Therefore, the proof is complete.

## APPENDIX B

### PROOF OF THEOREM 2: $\mathbf{A}_T^H(l_\tau, \mathbf{k}_\nu) \mathbf{A}_T(l_\tau, \mathbf{k}_\nu)$ CAN APPROXIMATE THE IDENTITY MATRIX

For convenience, the two columns in  $\mathbf{A}_T(l_\tau, \mathbf{k}_\nu)$  are denoted as  $\mathbf{a}_T(l_{\tau_1}, k_{\nu_1})$  and  $\mathbf{a}_T(l_{\tau_2}, k_{\nu_2})$ , respectively.  $|\mathbf{a}_T^H(l_{\tau_1}, k_{\nu_1}) \mathbf{a}_T(l_{\tau_2}, k_{\nu_2})|$  can be expressed as (68)-(73), as shown at the top of this page.

Simply substitute the corresponding terms to obtain (68). To obtain (69), we rearrange the order of the summations in (68) and group together all terms involving  $m$ . In (69), the summation over  $m$  equals 1 only when  $n_1 = n_2 = \bar{n}$ , and 0 otherwise. Thus, (69) simplifies

$$y(m) = \frac{1}{N} \sum_{\bar{n}=0}^{N-1} \sum_{i=1}^P h_i \sum_{n=0}^{N-1} x(n) e^{j2\pi(c_1(\bar{n}-l_{\tau_i})^2 + c_2 n^2 + \frac{(\bar{n}-l_{\tau_i})n}{N})} e^{\frac{j2\pi k_{\nu_i}}{N}(\bar{n}-l_{\tau_i})} e^{-j2\pi(c_1 \bar{n}^2 + c_2 m^2 + \frac{\bar{n}m}{N})} + w(m) \quad (65)$$

$$= \frac{1}{N} \sum_{\bar{n}=0}^{N-1} \sum_{i=1}^P h_i \sum_{n=0}^{N-1} x(n) e^{\frac{-j2\pi}{N}(2\bar{n}Nc_1 l_{\tau_i} - Nc_1 l_{\tau_i}^2 - Nc_2 n^2 - n\bar{n} + nl_{\tau_i} + (-k_{\nu_i} \bar{n} + k_{\nu_i} l_{\tau_i}) + (Nc_2 m^2 + \bar{n}m))} + w(m). \quad (66)$$

$$\begin{aligned} h_w(m, n) &= \frac{1}{N} \sum_{i=1}^P \sum_{\bar{n}=0}^{N-1} h_i e^{\frac{-j2\pi}{N}(2\bar{n}Nc_1 l_{\tau_i} - Nc_1 l_{\tau_i}^2 - Nc_2 n^2 - n\bar{n} + nl_{\tau_i} + (-k_{\nu_i} \bar{n} + k_{\nu_i} l_{\tau_i}) + (Nc_2 m^2 + \bar{n}m))} \\ &= \frac{1}{N} \sum_{i=1}^P h_i e^{\frac{-j2\pi}{N}(-Nc_1 l_{\tau_i}^2 + (n+k_{\nu_i})l_{\tau_i} + Nc_2(m^2 - n^2))} \sum_{\bar{n}=0}^{N-1} e^{\frac{-j2\pi}{N}(m-n+2Nc_1 l_{\tau_i} - k_{\nu_i})\bar{n}} \\ &= \sum_{i=1}^P h_i \alpha(m, n, l_{\tau_i}, k_{\nu_i}) \mathcal{F}(m, n, l_{\tau_i}, k_{\nu_i}). \end{aligned} \quad (67)$$

$$|\mathbf{a}_T^H(l_{\tau_1}, k_{\nu_1}) \mathbf{a}_T(l_{\tau_2}, k_{\nu_2})| = \left| \sum_{m=0}^{N-1} \frac{1}{N} \sum_{n_1=0}^{N-1} e^{\frac{j2\pi}{N}(m-n_p+2Nc_1 l_{\tau_1} - k_{\nu_1})n_1} \frac{1}{N} \sum_{n_2=0}^{N-1} e^{\frac{-j2\pi}{N}(m-n_p+2Nc_1 l_{\tau_2} - k_{\nu_2})n_2} \right| \quad (68)$$

$$= \frac{1}{N} \left| \sum_{n_1=0}^{N-1} \sum_{n_2=0}^{N-1} e^{\frac{-j2\pi}{N}[-n_p(n_2-n_1)+2Nc_1(l_{\tau_2}n_2-l_{\tau_1}n_1)-(k_{\nu_2}n_2-k_{\nu_1}n_1)]} \underbrace{\frac{1}{N} \sum_{m=0}^{N-1} e^{\frac{-j2\pi}{N}m(n_2-n_1)}}_{\delta(n_2-n_1)} \right| \quad (69)$$

$$= \frac{1}{N} \left| \sum_{\bar{n}=0}^{N-1} e^{\frac{-j2\pi}{N}[2Nc_1(l_{\tau_2}-l_{\tau_1})-(k_{\nu_2}-k_{\nu_1})]\bar{n}} \right| \quad (70)$$

$$= \frac{1}{N} \left| \frac{\sin\{\pi[2Nc_1(l_{\tau_2}-l_{\tau_1})-(k_{\nu_2}-k_{\nu_1})]\}}{\sin\{\frac{\pi}{N}[2Nc_1(l_{\tau_2}-l_{\tau_1})-(k_{\nu_2}-k_{\nu_1})]\}} \right| \quad (71)$$

$$\approx |\text{sinc}\{2Nc_1(l_{\tau_2}-l_{\tau_1})-(k_{\nu_2}-k_{\nu_1})\}| \quad (72)$$

$$\approx \left| \text{sinc} \left\{ \left( 2 \left( \frac{\nu_{\max}}{\Delta f} + \xi \right) + 1 \right) (\tau_2 - \tau_1) N \Delta f - (\nu_2 - \nu_1) \frac{1}{\Delta f} \right\} \right|. \quad (73)$$

to (70). Based on the result of the geometric series summation in (70), (71) can be obtained using Euler's formula. Since  $\frac{\pi}{N}(2Nc_1(l_{\tau_2}-l_{\tau_1})-(k_{\nu_2}-k_{\nu_1}))$  approaches 0, it leads to  $\sin\{\frac{\pi}{N}[2Nc_1(l_{\tau_2}-l_{\tau_1})-(k_{\nu_2}-k_{\nu_1})]\} \approx \frac{\pi}{N}[2Nc_1(l_{\tau_2}-l_{\tau_1})-(k_{\nu_2}-k_{\nu_1})]$ , thus yielding (72). By substituting (2) and (5) into (72), (73) is obtained.

For (72),  $|\mathbf{a}(l_{\tau_1}, k_{\nu_1})^H \mathbf{a}(l_{\tau_2}, k_{\nu_2})| = 1$  when  $l_{\tau_1} = l_{\tau_2}$  and  $k_{\nu_1} = k_{\nu_2}$ . For more general cases, since  $2Nc_1(l_{\tau_2}-l_{\tau_1})-(k_{\nu_2}-k_{\nu_1}) \gg 1$  in general,  $|\mathbf{a}(l_{\tau_1}, k_{\nu_1})^H \mathbf{a}(l_{\tau_2}, k_{\nu_2})|$  is close to 0. In addition, from (73), an increase in either  $\xi$  or  $N$  leads to  $2Nc_1(l_{\tau_2}-l_{\tau_1})-(k_{\nu_2}-k_{\nu_1})$  becoming greater than 1, which results in  $|\mathbf{a}(l_{\tau_1}, k_{\nu_1})^H \mathbf{a}(l_{\tau_2}, k_{\nu_2})|$  approaching 0 more closely. Therefore, this proof is completed.

### APPENDIX C PROOF OF THEOREM 3: $\left| \mathcal{T}^H(\hat{\gamma}_i + \gamma) \mathbf{y}_T \right|^2$ IS A BOUNDED UNIMODAL FUNCTION

The proof of Theorem 3 can be seen in (74)-(77), as shown at the top of the next page. Since  $\mathbf{a}_T(l_{\tau_i}, k_{\nu_i})$  and  $\mathcal{T}^H(\hat{\gamma}_i + \gamma)$  have the same structure, substituting  $\mathbf{y}_T = \sum_{j=1}^P x_p h_i \mathbf{a}_T(l_{\tau_j}, k_{\nu_j})$  and considering the orthogonality of  $\mathbf{a}_T(l_{\tau_i}, k_{\nu_i})$  yields (74). Considering that the  $c_2$  is small enough, (75) can be obtained. Similar to the derivation process of (68)-(71) in the Appendix B, (75) can be written as (76). Since  $\hat{\gamma}_i - \gamma_i \approx 0$ , which leads to (77). In addition,  $\gamma - \gamma_i \in [-1, 1]$ . Therefore,  $\left| \mathcal{T}^H(\hat{\gamma}_i + \gamma) \mathbf{y}_T \right|^2$  is a bounded unimodal function, with its extremum achieved at  $\gamma = \gamma_i$ .

Therefore, this proof is completed.

$$\left| \mathcal{T}^H \left( \hat{\gamma}_i + \gamma \right) \mathbf{y}_T \right|^2 \approx \left| x_p h_i \mathcal{T}^H \left( \hat{\gamma}_i + \gamma \right) \mathbf{a}_T(l_{\tau_i}, k_{\nu_i}) \right|^2 \quad (74)$$

$$\approx \left| x_p h_i \mathcal{T}^H \left( \hat{\gamma}_i + \gamma \right) \mathcal{T}^H (\gamma_i + \gamma_i) \right|^2 \quad (75)$$

$$\approx \left| \frac{1}{N} x_p h_i \frac{\sin \left\{ \pi \left[ \hat{\gamma}_i - \gamma_i + \gamma - \gamma_i \right] \right\}}{\sin \left\{ \frac{\pi}{N} \left[ \hat{\gamma}_i - \gamma_i + \gamma - \gamma_i \right] \right\}} \right|^2 \quad (76)$$

$$\approx |x_p h_i| \sin c(\gamma - \gamma_i) \quad (77)$$

## REFERENCES

- [1] T. Wang, J. G. Proakis, E. Masry, and J. R. Zeidler, "Performance degradation of OFDM systems due to Doppler spreading," *IEEE Transactions on Wireless Communications*, vol. 5, no. 6, pp. 1422–1432, Jun. 2006.
- [2] L. Rugini and P. Banelli, "BER of OFDM systems impaired by carrier frequency offset in multipath fading channels," *IEEE Transactions on Wireless Communications*, vol. 4, no. 5, pp. 2279–2288, Sep. 2005.
- [3] M. Noor-A-Rahim, Z. Liu, *et al.*, "6G for vehicle-to-everything (V2X) communications: Enabling technologies, challenges, and opportunities," *Proceedings of the IEEE*, vol. 110, no. 6, pp. 712–734, Jun. 2022.
- [4] R. Hadani *et al.*, "Orthogonal time frequency space modulation," *2017 IEEE Wireless Communications and Networking Conference (WCNC)*, San Diego, CA, USA, Mar. 2017, pp. 1–6.
- [5] R. Hadani *et al.*, "Orthogonal time frequency space (OTFS) modulation for millimeter-wave communications systems," *2017 IEEE MTT-S International Microwave Symposium (IMS)*, Honolulu, HI, USA, Jun. 2017, pp. 681–683.
- [6] Z. Wei *et al.*, "Orthogonal time-frequency space modulation: a promising next-generation waveform," *IEEE Wireless Communications*, vol. 28, no. 4, pp. 136–144, Aug. 2021.
- [7] P. Raviteja, K. T. Phan, Y. Hong, and E. Viterbo, "Interference cancellation and iterative detection for orthogonal time frequency space modulation," *IEEE Transactions on Wireless Communications*, vol. 17, no. 10, pp. 6501–6515, Oct. 2018.
- [8] S. Li, J. Yuan, W. Yuan, Z. Wei, B. Bai and D. W. K. Ng, "Performance analysis of coded OTFS systems over high-mobility channels," *IEEE Transactions on Wireless Communications*, vol. 20, no. 9, pp. 6033–6048, Sept. 2021.
- [9] P. Raviteja, K. T. Phan and Y. Hong, "Embedded pilot-aided channel estimation for OTFS in delay–Doppler channels," *IEEE Transactions on Vehicular Technology*, vol. 68, no. 5, pp. 4906–4917, May 2019.
- [10] Z. Wei, W. Yuan, S. Li, J. Yuan, and D. W. K. Ng, "Off-grid channel estimation with sparse Bayesian learning for OTFS systems," *IEEE Transactions on Wireless Communications*, vol. 21, no. 9, pp. 7407–7426, Sep. 2022.
- [11] Q. Wang, Y. Liang, Z. Zhang, and P. Fan, "2D off-grid decomposition and SBL combination for OTFS channel estimation," *IEEE Transactions on Wireless Communications*, vol. 22, no. 5, pp. 3084–3098, May 2023.
- [12] X. Li, P. Fan, Q. Wang, and Z. Liu, "Grid evolution for doubly fractional channel estimation in OTFS systems," *IEEE Transactions on Vehicular Technology* (Early Access), pp. 1–5, 2024.
- [13] A. Bemani, N. Ksairi, and M. Kountouris, "AFDM: a full diversity next generation waveform for high mobility communications," *2021 IEEE International Conference on Communications Workshops (ICC Workshops)*, Jun. 2021, pp. 1–6.
- [14] A. Bemani, G. Cuzzo, N. Ksairi, and M. Kountouris, "Affine frequency division multiplexing for next-generation wireless networks," *2021 17th International Symposium on Wireless Communication Systems (ISWCS)*, Sep. 2021, pp. 1–6.
- [15] A. Bemani, N. Ksairi, and M. Kountouris, "Affine frequency division multiplexing for next generation wireless communications," *IEEE Transactions on Wireless Communications*, vol. 22, no. 11, pp. 8214–8229, Nov. 2023.
- [16] T. Erseghe, N. Laurenti and V. Cellini, "A multicarrier architecture based upon the affine Fourier transform," *IEEE Transactions on Communications*, vol. 53, no. 5, pp. 853–862, May 2005.
- [17] X. Ouyang and J. Zhao, "Orthogonal chirp division multiplexing," *IEEE Transactions on Communications*, vol. 64, no. 9, pp. 3946–3957, Sep. 2016.
- [18] E. Başar, Ü. Aygölü, E. Panayircı, and H. V. Poor, "Orthogonal frequency division multiplexing with index modulation," *IEEE Transactions on Signal Processing*, vol. 61, no. 22, pp. 5536–5549, Nov. 2013.
- [19] Y. Tao, M. Wen, Y. Ge, and J. Li, "Affine frequency division multiplexing with index modulation," *2024 IEEE Wireless Communications and Networking Conference (WCNC)*, Apr. 2024, pp. 1–6.
- [20] J. Zhu, Q. Luo, G. Chen, P. Xiao, and L. Xiao, "Design and performance analysis of index modulation empowered AFDM system," *IEEE Wireless Communications Letters*, vol. 13, no. 3, pp. 686–690, Mar. 2024.
- [21] G. Liu, T. Mao, R. Liu, and Z. Xiao, "Pre-Chirp-Domain Index Modulation for Affine Frequency Division Multiplexing," *2024 International Wireless Communications and Mobile Computing (IWCMC)*, Ayia Napa, Cyprus, May, 2024, pp. 0473–0478.
- [22] H. S. Rou, K. Yukiyoishi, T. Mikuriya, G. T. F. de Abreu, and N. Ishikawa, "AFDM chirp-permutation-index modulation with quantum-accelerated codebook design," May 2024, [online]: <https://arxiv.org/abs/2405.02085>.
- [23] Z. Sui, Z. Liu, L. Musavian, L.-L. Yang, and L. Hanzo, "Generalized spatial modulation aided affine frequency division multiplexing," Jan. 2025, [online]: <https://arxiv.org/abs/2501.10865>.
- [24] Y. Ni, Z. Wang, P. Yuan, and Q. Huang, "An AFDM-based integrated sensing and communications," *2022 International Symposium on Wireless Communication Systems (ISWCS)*, Hangzhou, China: IEEE, Oct. 2022, pp. 1–6.
- [25] A. Bemani, N. Ksairi, and M. Kountouris, "Integrated sensing and communications with affine frequency division multiplexing," *IEEE Wireless Communications Letters*, vol. 13, no. 5, pp. 1255–1259, May 2024.
- [26] J. Zhu, Y. Tang, F. Liu, X. Zhang, H. Yin, and Y. Zhou, "AFDM-based bistatic integrated sensing and communication in static scatterer environments," *IEEE Wireless Communications Letters*, vol. 13, no. 8, pp. 2245–2249, Aug. 2024.
- [27] Q. Luo, P. Xiao, Z. Liu, Z. Wan, N. Thomos, Z. Gao, and Z. He, "AFDM-SCMA: A promising waveform for massive connectivity over high mobility channels," *IEEE Trans. Wireless Commun.*, vol. 23, no. 10, pp. 14421–14436, Oct. 2024.
- [28] H. Yin and Y. Tang, "Pilot aided channel estimation for AFDM in doubly dispersive channels," *2022 IEEE/CIC International Conference on Communications in China (ICCC)*, Aug. 2022, pp. 308–313.
- [29] W. Benzine, A. Bemani, N. Ksairi, and D. Stock, "Affine frequency division multiplexing for compressed sensing of time-varying channels," *2024 IEEE 25th International Workshop on Signal Processing Advances in Wireless Communications (SPAWC)*, Sep. 2024, pp. 916–920.
- [30] W. Benzine, A. Bemani, N. Ksairi, and D. Stock, "Affine frequency division multiplexing for communications on sparse time-varying channels," *GLOBECOM 2023 - 2023 IEEE Global Communications Conference*, Dec. 2023, pp. 4921–4926.
- [31] F. Yang, S. Luo, L. Wu, D. Song, R. Lin and S. Xie, "An AFDM off-grid channel estimation based on sparse Bayesian learning," *IEEE 24th International Conference on Communication Technology (ICCT)*, Chengdu, China, 2024, pp. 1565–1569.
- [32] H. Yin, X. Wei, Y. Tang, and K. Yang, "Diagonally reconstructed channel estimation for MIMO-AFDM with inter-Doppler interference in doubly selective channels," *IEEE Transactions on Wireless Communications* (Early Access), 2024.
- [33] G. Matz, "On non-WSSUS wireless fading channels," *IEEE Transactions on Wireless Communications*, vol. 4, no. 5, pp. 2465–2478, Sept. 2005.
- [34] Khan I A, Mohammed S K, "Low complexity channel estimation for OTFS modulation with fractional delay and Doppler". Nov, 2021, [online]: <https://arxiv.org/abs/2111.06009>.
- [35] M. Avriel and D. J. Wilde, "Optimality proof for the symmetric Fibonacci search technique," *The Fibonacci Quarterly*, vol. 4, no. 3, pp. 265–269, Oct. 1966.
- [36] M. Subasi *et al.*, "An improvement on Fibonacci search method in optimization theory," *Applied Mathematics and Computation*, vol. 147, no. 3, pp. 893–901, Jan. 2004.
- [37] C. Y. Chong *et al.*, "Generalized Fibonacci search method in one-dimensional unconstrained non-linear optimization," *Pertanika Journal of Science and Technology*, vol. 29, no. 2, Apr. 2021.
- [38] D. Tse and P. Viswanath, "Fundamentals of Wireless Communication," Cambridge, U.K.: Cambridge Univ. Press, 2005.